Catalysis Science & Technology

# Developing a Microwave-Driven Reactor for Ammonia Synthesis: Insights into the Unique Challenges of Microwave Catalysis



| | |
|---|---|
| Journal: | *Catalysis Science & Technology* |
| Manuscript ID | CY-ART-12-2022-002181.R1 |
| Article Type: | Paper |
| Date Submitted by the Author: | 23-Feb-2023 |
| Complete List of Authors: | Melkote, Sunjay; Malachite Technologies Inc<br>Muley, Pranjali; National Energy Technology Laboratory Morgantown<br>Dutta, Biswanath; National Energy Technology Laboratory Morgantown<br>Wildfire, Christina; National Energy Technology Laboratory Morgantown<br>Weiss, Robert; Malachite Technologies Inc<br>Hu, Jianli; West Virginia University, Chemical and Biomedical Engineering |
| | |

# Developing a Microwave-Driven Reactor for Ammonia Synthesis: Insights into the Unique Challenges of Microwave Catalysis

Sunjay G Melkote[1*], Pranjali Muley[2, 3], Biswanath Dutta[2, 3], Christina Wildfire[2], Robert Weiss[1], Jianli Hu[4]

[1] Malachite Technologies, Inc., San Francisco, CA, USA

[2] National Energy Technology Laboratory, 3610 Collins Ferry Road, Morgantown, WV 26505 USA

[3] NETL Support Contractor, 3610 Collins Ferry Road, Morgantown, WV 26505, USA

[4] West Virginia University, Morgantown, WV, USA

[*] Corresponding author. Email: *smelkote@malachitetech.com*

## Abstract

Rapid development of new ammonia ($NH_3$) synthesis techniques that enable modular, intermittent production is essential to actualizing $NH_3$'s potential as a clean energy carrier, since contemporary methods are configured to centralized, continuous production methods with high emissions and are incompatible with renewable sources. In this mission, microwave-driven catalysis is promising for its ability to enhance reaction kinetics and apply targeted heating for efficient energy use. However, owing to an incomplete understanding of the interaction between microwave fields and catalyst beds, the development of such microwave-catalysis systems remains underexplored and challenging. This paper investigates the 10x scale-up of a microwave-based $NH_3$ synthesis reactor using numerical and experimental approaches, achieving the largest reported microwave-driven $NH_3$ reactor to date. Results elucidate phenomena unique to microwave processes that are only predictable through numerical modeling, including how a catalyst's dielectric properties influence microwave field distribution by affecting penetration depth and how energy utilization can be poor even with sufficient attenuation. These dynamics change with scale, constrain reactor geometry, and potentially hamper performance. Nonetheless, we demonstrate a production rate of 56.6 $g_{NH3}$/day, the highest reported $NH_3$ synthesis rate for laboratory-scale alternative techniques; correspondingly, the benchmark energy efficiency achieved in this paper (45.6 $g_{NH3}$/kWh) is the highest reported for such reactors of sufficient scale. Even with this exemplary energy efficiency, energy losses were found in excess of 50%, an issue resolvable through scale and reactor design. The efficiencies imparted by microwaves were key in these achievements, warranting further investigation toward development of microwave-driven $NH_3$ systems.

## 1 Introduction

The energy crisis is one of the world's greatest challenges, with harmful externalities ranging from geopolitics to climate change. To tackle this problem, ample focus has been placed on developing a diverse set of technologies that can generate clean energy, including optimizing the performance and durability of solar panels[1, 2] or advancing the utility of wind turbines.[3] While harvesting technology has advanced considerably, energy storage remains underdeveloped.[4] One promising solution is the storage of energy in liquid ammonia ($NH_3$). Specifically, $NH_3$ has a fairly high volumetric energy density (7.1 MJ/L, higher than alternatives like batteries), exceptional hydrogen carrying density (more than liquid hydrogen itself), and respectable carbon-free combustion properties.[5] Since it condenses at relatively modest conditions (about 10 bar at room temperature or -33°C at ambient pressure), the cost of $NH_3$ storage and transportation is significantly lower than alternatives like hydrogen, batteries, or others.[6] Moreover, long distance $NH_3$ transport by pipeline is far more economically feasible than electrical transmission lines, which lose power in transit at least 5 times faster than $NH_3$ pipelines due to transmission power losses.[7] Developing $NH_3$-for-energy systems is critical to realizing this use.

$$3H_2(g) + N_2(g) \rightleftharpoons 2NH_3(g) \qquad \Delta H_{298\,K} = -165 \text{ kJ mol}^{-1} \qquad \text{Eq. 1}$$

Over 96% of $NH_3$ produced today is generated by the well-developed Haber-Bosch (HB) process,[8] which uses an iron-based catalyst to facilitate the reduction of gaseous dinitrogen ($N_2$) with gaseous dihydrogen ($H_2$) to form $NH_3$ (**Equation 1**). While greater equilibrium conversion to $NH_3$ occurs at higher pressures and lower temperatures, immense thermal energy is still required to break the very stable N-N triple bond (N≡N) in $N_2$.[9] High temperatures are, therefore, required kinetically for faster reaction rates. As such, traditional HB plants operate at high temperatures (about 400°C – 500°C) to enhance the $NH_3$ synthesis rate, compensating for the resulting low equilibrium with high operating pressures (about 200 bar – 400 bar).[9] These intense conditions create substantial capital and operating expenses that necessitate maximal production for economic feasibility. This, unfortunately, has driven plants to large and centralized production with continuous, low turn-down operation and an insensitivity to changing conditions,[10] antithetical to common renewable energy harvesting techniques that are inherently geographically dispersed with variable operating loads. As a result, they still require hydrocarbon feedstock to generate $H_2$ precursor. Consequently, $NH_3$ production consumes up to 2% of global energy and emits over 1% of global emissions (about 620 $Mtonne_{CO2}$/yr, or 3 $tonne_{CO2}/tonne_{NH3}$), both more than any other produced chemical.[11, 12] Therefore, a production method that can viably operate with an intermittent power supply on a scale smaller than Haber-Bosch is necessary.

To date, several innovative techniques have been explored, primarily including electrochemical and plasma-assisted synthesis.[13, 14] Although promising, each has significant shortcomings. Electrochemical

methods suffer from low $NH_3$ yields[14] despite offering some of the mildest reported reaction conditions with high energy efficiencies. Conversely, plasma-assisted synthesis is far less energy efficient, limiting its potential for commercialization.[13] As a result, little work on the scale-up and intensification of these processes has been reported.

Non-plasma microwave field-assisted synthesis is a promising alternative. Microwave irradiation can instantaneously and selectively heat catalysts and support materials, where the electromagnetic energy translates directly into molecular kinetic energy in the absorber without heating the microwave-transparent reacting gas.[15] Extended X-ray Absorption Fine Structure (EXAFS) measurements also suggest that microwaves can selectively heat metallic nanoparticle active sites in a catalyst, leaving the bulk support material at a much lower temperature.[16] This selective heating can eliminate side reactions by allowing the inlet and outlet gas streams to remain cool while only reaction sites are heated. This is particularly important in $NH_3$ synthesis, as $N_2$ gas can react with certain metals (e.g., the process vessels) around 500°C and thermal $NH_3$ decomposition starts around 500°C – 600°C.[9, 17] Properly tuned microwave fields can also heat the entire volume of a sample uniformly to simultaneously deliver energy across a material's entire body (known as "volumetric heating"), whereas traditional heating processes require thermal conduction or convection from hot surfaces. This significantly improves processing time to enable efficient, dynamic, and intermittent operation that can follow startup and shutdown patterns of renewable energy sources.[18] Additionally, through work done by this group, microwave irradiation has been shown to both facilitate electron transfer between catalysts and reaction intermediates[19] and reduce activation energy by assisting in the rate-limiting cleavage of the $N_2$ triple bond.[20] These mechanistic enhancements have allowed high reaction rates at lower reaction temperatures (below 300°C) in the presence of a microwave field.[21] Operation at a lower temperature can enable work at lower pressure: reaction in the 260°C – 360°C and 20 bar – 30 bar temperature and pressure ranges has an average equilibrium conversion of about 42%, similar to Haber-Bosch's 39% equilibrium conversion but at far milder conditions.[22] These factors can reduce expenses and enable small-scale, distributed, modular operation that can load-follow with intermittent renewable sources.

Existing work in this effort has been limited to a laboratory-benchtop scale with, at most, 1 g of active catalyst.[23, 24] However, an often-overlooked challenge involves the scale-up of novel technologies that have yet to achieve significant scale. Indeed, methodologies for scaling-up known techniques are already well-developed.[25] With novel technologies, such frameworks are often unexplored or nonexistent, and factors deemed negligible on a small scale can grow to dominate and hamper larger systems. Specifically, there are several unique aspects of microwave systems that dictate operation, including attenuation and penetration depth, resonance and field distribution, and heating efficiency, to name a few.[26]

Additionally, while heating through electromagnetic fields has a high potential for uniform temperature distribution, achieving such uniformity in practice requires a large amount of engineering to properly tune the fields, absorbing materials, and reactor geometry. Reaction conditions, like gas flow or heat contributions from exothermic or endothermic reactions, add further layers of complication, especially during dynamic operation. These factors all can vary with scale in a poorly understood way and rely on material and process parameters that are either difficult or impossible to measure, making the set of relevant process parameters difficult to predict or observe with modeling or experimentation alone.[27] In this scenario, it is essential to pair experimentation with numerical modeling to overcome the limitations of one another and guide further development.

In this work, we demonstrate the initial 10x scale-up of a non-plasma microwave reactor module and evaluate how this effort can provide insight into further scaling. We do this by combining both numerical and experimental approaches to describe how variables like microwave field distribution and attenuation can contradict prediction and influence reactor performance. Additionally, we optimize these parameters to achieve higher $NH_3$ production and energy efficiencies, thereby gauging both its amenability to further scale-up to a full-scale process and what analytic principles such development should follow.

## 2 Results & Discussion

To begin scale-up, a modular H-Field microwave reactor system was designed and fabricated by Malachite Technologies, Inc (**Figure S1**, ESI). This allowed heating larger amounts of catalyst than previously investigated[23, 24] using $TE_{10}$ and $TM_{010}$ microwave heating modes, which impart enhanced heating uniformity through various catalyst loads. The reactor suspends the catalyst bed in the cavity using a quartz tube (necessary as a microwave-transparent material) and subjects it to microwave heating. Correspondingly, a model of the H-Field reactor was constructed using COMSOL Multiphysics (**Figure S1**, ESI). The most direct way to quantify a microwave field's distribution in a catalytic reactor is to measure the resulting temperature distribution in its catalyst bed. However, this can be prohibitively difficult with conventional tools. For example, metallic thermocouples can interact with microwave fields, falsely skewing the measurement or even altering the field distribution itself.[28] Additionally, thermal imaging devices can fail to accurately capture temperature profiles for these system due to visual distortions that can become prevalent during operation. For example, thermal reflections are known to skew measurement when imaging low emissivity materials,[29] and such reflections are likely with quartz under harsh conditions as its emissivity drops as its temperature increases[30] (**Section S2**, ESI). As such, numerical modeling is required to enhance the understanding of the microwave field's variation with scale and establish a framework to guide experimentation.

### 2.1 Catalyst Characterization

Evaluation of certain catalyst properties is necessary to begin modeling and experimentation. Ru-based catalysts are common in the field of $NH_3$ synthesis for various experimental and industrial applications, primarily for its ability to promote $N_2$ activation and incite reduction to $NH_3$.[20] This group has developed a Ru catalyst that has been enhanced by support- and promoter-effects.[23] Particularly, Cs was incorporated as a promoter for its electron-donating ability,[31] and microkinetic modelling found that Cs was the optimal promoter in maximally reducing the free energy of $N_2$ cleavage (the rate-limiting step of the reaction).[20] $CeO_2$ was used as a support material for both its reversible $Ce^{3+}/Ce^{4+}$ transformation and its abundance of oxygen vacancies, both of which enhance Ru surface electron density and promote conversion to $NH_3$.[32] A composition of 2 wt.% Cs and 4 wt.% Ru supported on $CeO_2$ experimentally exhibits optimal activity in a microwave field, and full characterization of this catalyst composition has been reported in previous work by this group.[23] This CsRu2-4%/$CeO_2$ catalyst will be the catalyst used for the entirety of this paper. Scanning electron microscope (SEM) imaging of this catalyst (**Figure 1a**) reveals a significantly rough and porous surface, which is ideal for heterogeneous solid-gas phase catalyst.

Dielectric properties of this catalyst were measured using a perturbation technique to evaluate the interaction between this catalyst and the microwave field (relevant equations[33] can be found in **Section S3**, ESI). The complex permittivity of a material governs its interaction with microwave fields and has two components: the real portion (the dielectric constant, $\varepsilon'$) and the imaginary portion (the loss index, $\varepsilon''$). The former is a measure of a material's ability to store energy, while the latter measures a material's ability to convert electrical energy into heat.[33] Both $\varepsilon'$ and $\varepsilon''$ were measured for the catalyst under microwave irradiation. Samples first underwent a 1 hr reduction at 260°C in a reducing atmosphere (4% $H_2$ in Ar), followed by a progressive linear sweep in temperature (°C) from 25°C to 600°C (**Figure 1b** in red circles and blue squares, respectively). The relatively constant value of $\varepsilon'$ throughout the temperature range indicates the catalyst's stability and an unchanged energy storage capacity, while the rapid increase in $\varepsilon''$ with temperature indicates the conversion of microwave energy to heat becomes easier with temperature. The loss tangent, $\tan\delta$, is the ratio of the loss index to the dielectric constant and represents how well microwave energy is absorbed by a material.[33] In this case, the loss tangent increases significantly with temperature. Since dielectric constant is relatively stable throughout the temperature range, this increase can be ascribed to an enhanced ability to convert the field energy into thermal energy at higher temperatures.

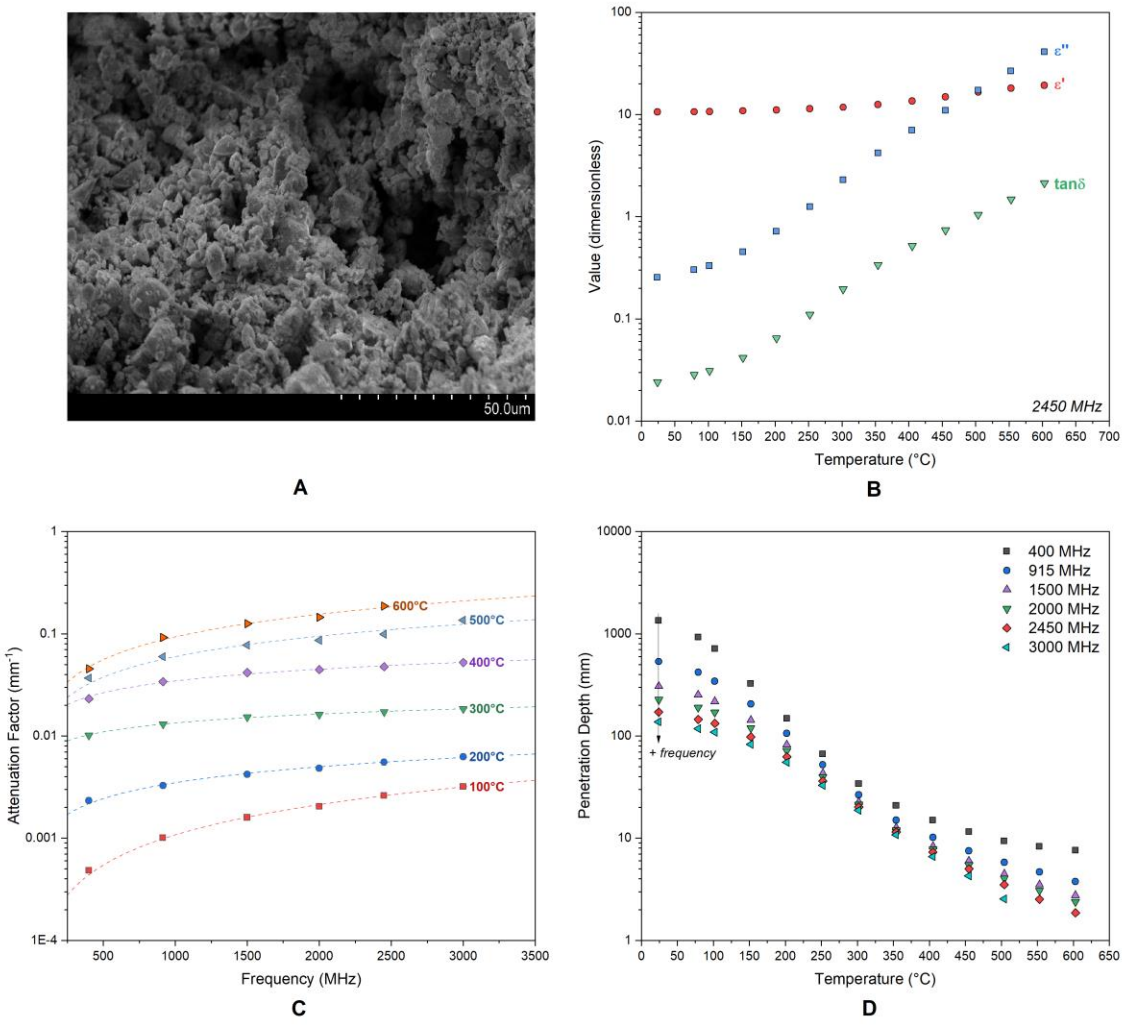


**Figure 1.** (**A)** SEM image of the porous CsRu2-4%/$CeO_2$ catalyst structure. (**B**) Dielectric properties of CsRu2-4%/$CeO_2$ through a linear temperature sweep between 25°C and 600°C, including dielectric constant (ε′), loss index (ε″), and loss tangent (tanδ) at a 2450 MHz frequency. (**C**) Attenuation factor (α, measured in $mm^{-1}$) of various isotherms under varying frequency. Simple curve fits are displayed (dashed lines) for illustrative purposes. (**D**) Penetration depth (mm) of various frequencies (400 MHz, 915 MHz, 1500 MHz, 2000 MHz, 2450 MHz, 3000 MHz) at various temperatures. Note that penetration depth reported here is represented by half-power penetration depth (**Section S3**, ESI).

The attenuation factor, α, measures the rate of absorption into a material and varies as a function of the dielectric constant and loss tangent. Attenuation was computed for varying frequencies and evaluated for several different temperatures (**Figure 1c**). Consistent with findings in **Figure 1b**, absorption is

facilitated by higher temperatures at all frequencies. Importantly, at all temperatures, an increase in frequency consistently increased attenuation. However, significantly high attenuation can be limiting to scale-up and reactor development. Indeed, while microwave heating can be thought of as "volumetric," this is a simplification: microwave absorption in a sample starts with initial irradiation around the perimeter of the absorbing sample and progresses inward (**Figure S3**, ESI).[34] Extremely high attenuation at exceedingly high frequency can lead to surface heating alone, resulting in a very poor distribution. This is evident with each frequency's penetration depth (**Figure 1d**), which is proportional to the inverse of a material's attenuation.[33] Since the present reactor system operates with a cylindrical catalyst bed (**Figure S1**, ESI), this microwave penetration (with the $TM_{010}$ heating mode) will progress uniformly from the perimeter of the cylinder to the core. Penetration depth decreases monotonically with temperature as a result of increased attenuation. Higher frequencies experience less penetration for the same reason.

This has critical implications to scale-up. Penetration depth can suffer if operating temperature gets too high, resulting in incomplete activity in the catalyst bed. Moreover, the primary benefit of lower frequency is the increased penetration, offering the ability to penetrate further into wider catalyst beds. However, with smaller catalyst beds at laboratory scale, it is important to ensure all energy is attenuated into a sample to ensure optimal energy utilization. Foregoing this for increased penetration could result in wasted energy. As such, higher frequency is most appropriate for this scale even though it constrains tube diameter. It is also important to note that specific electromagnetic frequencies are restricted for specific applications. In the United States, for example, frequency for industrial, scientific, or medical applications is limited to two ranges in the tested set (915 MHz ± 13 MHz and 2450 MHz ± 50 MHz), limiting what is applicable to a scaled system.[35] These two ranges represent a step change in frequency, with significantly different field properties. As such, a frequency of 2450 MHz was used for the entirety of this work. The average penetration depth at this frequency for this work's operating temperature regime (260°C – 360°C) is about 16 mm.

## 2.2 Numerical Modeling

Since average penetration depth through the $CeO_2$-based catalyst at 2450 MHz frequency in the reactor's operating regime is about 16 mm and microwave penetration occurs around the perimeter of the tube, tube diameter is limited to 32 mm. Informed by measured dielectric properties, we developed a COMSOL model and studied the electric field intensity and temperature profiles in two reactor tube diameters (13 mm and 26 mm), well within the ideal penetration limit to account for the variation of penetration with temperature (**Figure 2**). These models do not account for exothermic contributions from the $NH_3$ synthesis reaction. Two bed heights (76.2 mm and 279.4 mm) were considered for each diameter. Each case was modeled under a gas-hourly space velocity (GHSV, a measure of space velocity depicting

the ratio of volumetric gas flow at STP to catalyst bed volume) of around 1,400 $hr^{-1}$ for the 76.2 mm tall cases and about 8,000 $hr^{-1}$ for the 279.4 mm cases. These GHSVs ensure a constant linear velocity (125 mm/s) among all tests. Since thermal mass changes and each point in the bed has the same attenuation capacity, the reactor tube diameter has a significant influence on where absorption is most dominant. At a 13 mm diameter with 76.2 mm height (**Figure 2a**), field penetration occurs through the bed with progressive inward attenuation, resulting in a relatively uniform distribution with slight concentration at the core of the column. As the bed diameter is increased to 26 mm (**Figure 2c**), attenuation is less uniform and regions with close to no attenuation exist. As bed height gets larger (**Figure 2b** and **Figure 2d** for the 13 mm and 26 mm tubes, respectively), the field becomes increasingly concentrated in the vertical center of the bed and significant portions of the catalyst bed experience no microwave field penetration (more so for the 26 mm tube than the 13 mm tube). Additionally, for the 13-by-279.4 mm, 26-by-76.2 mm, and 26-by-279.4 mm test cases (which all have significantly more thermal mass than the 13-by-76.2 mm case), there is significant field attenuation left-of-center in each bed, closest to the microwave power source (**Figure S1**). This is a result of the field distribution inherent to this reactor's geometry with large thermal masses, and it indicates that field distribution can deviate from ideal predicted behavior under these circumstances. These findings indicate there are significant geometric constraints, beyond what can be predicted with penetration depth, that can only be revealed through numerical modeling.

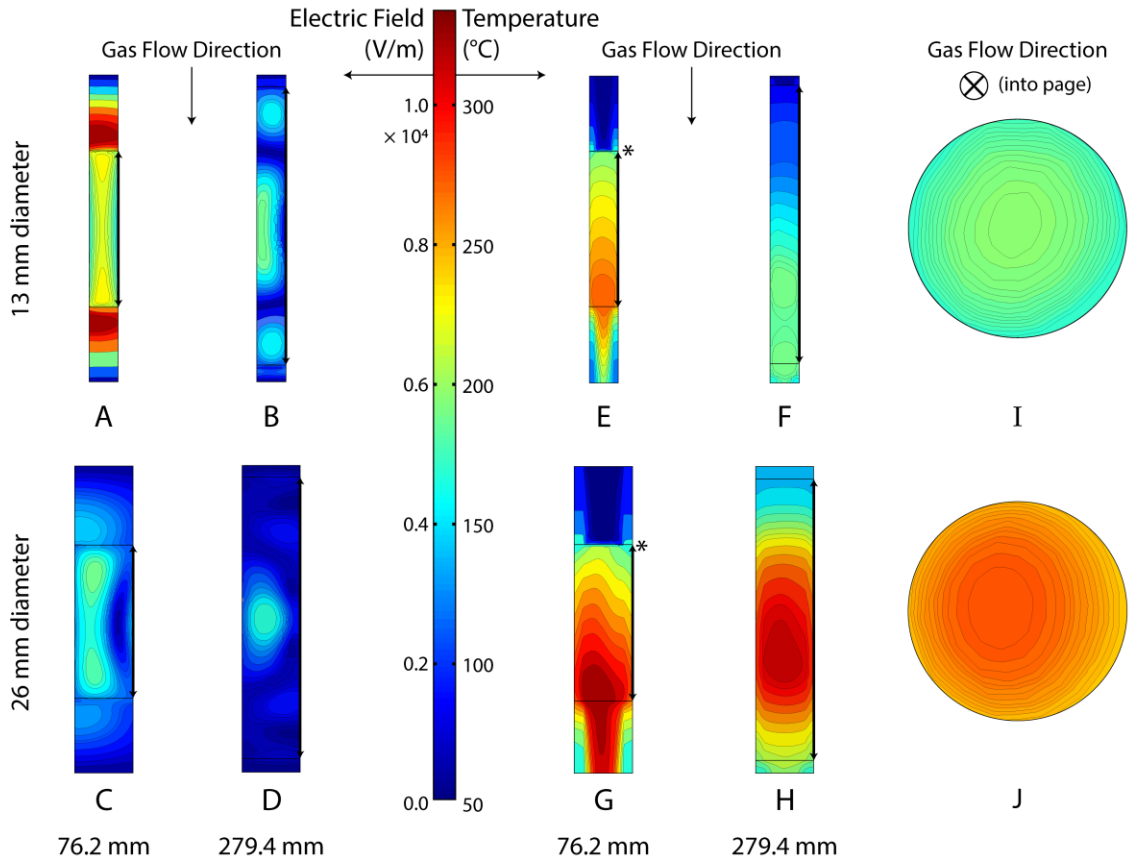


**Figure 2.** Cross-sections of electric field (V/m) profiles in reactor tube containing (**A**) a 13 mm diameter by 76.2 mm tall bed, (**B**) a 13-by-279.4 mm bed, (**C**) a 26-by-76.2 mm bed, and (**D**) a 26-by-279.4 mm bed. Cross-sections of temperature (°C) profiles in (**E**) a 13-by-76.2 mm tall bed, (**F**) a 13-by-279.4 mm tall bed, (**G**) a 26-by-76.2 mm tall bed, and (**H**) a 26-by-279.4 mm tall bed. Bed locations within each tube are denoted at the inlet and outlet, with span signified by an arrow along the wall. Corresponding inlet radial temperature profiles (top plane) in the (**I**) 13 mm-by-76.2 mm bed height and (**J**) 26-by-76.2 mm bed height reactor models, location denoted by an asterisk (*). Microwave field were modeled at 2450 MHz frequency. Note that each image was mapped to a common discrete color scale for clarity, corresponding to both electric field (left of the scale) and temperature profiles (right). Original COMSOL images can be found in **Figure S4** (**Section S5**, ESI).

In the absence of other factors, these attenuation profiles could result in matching temperature profiles, where the larger-mass cases experience hotspot formation with a radial bias toward the power source. However, since the catalyst material is highly conductive, the temperature profile is dominated by the high gas velocities. In the 13-by-76.2 mm and 26-by-76.2 mm tubes (**Figure 2e** and **Figure 2g**, respectively), this results in sufficiently uniform radial temperature profiles (**Figure 2i** and **Figure 2j**) that are in good agreement with the experimental thermal data in the absence of reaction (**Figure S2**, ESI). However, the temperature gradient in the axial direction becomes significant and potentially hampering to

operation. This is especially true at larger bed heights. In **Figure 2f**, for example, the temperature range in the 13-by-279.4 mm bed is 40°C – 185°C, which is significantly higher than the corresponding range in the 76.2 mm bed, where the range is 190°C – 280°C (**Figure 2e**). Doubling the tube diameter can effectively pack more catalyst closer to the center, alleviating some of the impact of increased height. Specifically, the 26-by-76.2 mm bed (**Figure 2g**) holds about the same volume as the 13-by-279.4 mm bed (40.5 mL vs 37.1 mL, respectively) and the length of its temperature range is comparable (200°C – 350°C), but total attenuation is superior (seen in the higher temperature of the range). There is, however, a limit to this increased packing efficiency, as the temperature range in the 26-by-279.4 mm tube (**Figure 2h**) increases to 100°C – 329°C.

This investigation of bed height was extended under gas flow. Increasing gas flow has a significant cooling effect on the temperature profile in the reactor (**Figure S5**, ESI), where higher flow rates carry heat away from the catalyst and shift the hotspots toward the bottom of the bed. In this way, the flowing reactant gas also acts as a cooling gas and necessitates higher microwave powers to reach the same temperatures, in agreement with experimental results discussed later (**Table S1**, ESI). As such, volumetric gas flow rate was kept constant at 1 slm (GHSV decreased due to the increasing volume), and field intensity was maximized (**Figure 3**). Catalyst bed heights of 19 mm, 38.1 mm, 76.2 mm, 101.6 mm, and 279.4 mm were tested in the 13 mm tube. The temperature profiles follow a similar pattern in all catalyst bed heights, where gas cooling at the inlet lowers the temperature at the top end of the bed and the progressive heat exchange between the flowing gas and hot catalyst causes a carry-through that raises the temperature at the bottom. The model results were in good agreement with experimental measurements of the surface temperature for 13-by-19 mm bed height at 260°C (the model recorded 263°C). The temperature gradient inside the catalyst bed increases as the bed height increases since longer bends offer a longer path for conductive and convective heat transfer, compounding any non-uniformity imparted by more thermal mass, with the smallest temperature gradient in the 19 mm catalyst bed and the largest gradient in the 279.4 mm bed. This is most notable in the tallest (279.4 mm) case, where the entirety of the bed was below 200°C (**Figure S6**).

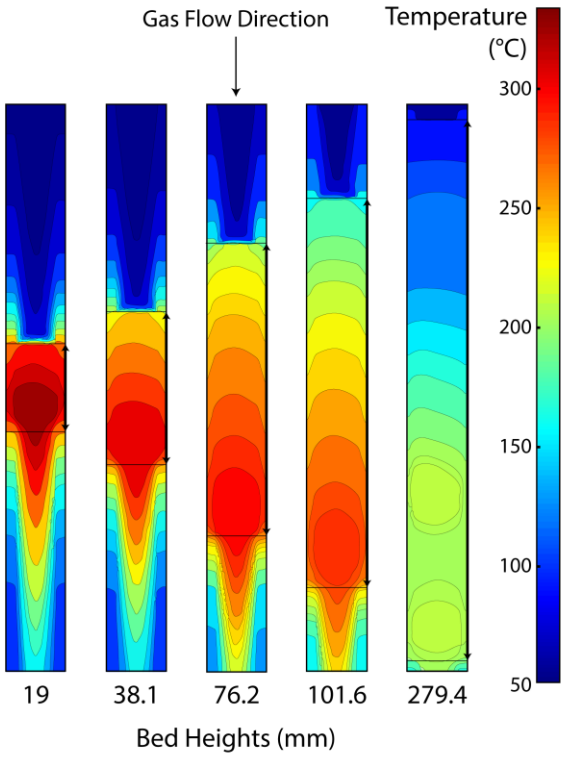


**Figure 3.** Cross-sections of temperature profiles inside the 13 mm reactor tube for varying catalyst bed heights (19 mm, 38.1 mm, 76.2 mm, 101.6 mm, and 279.4 mm), under equivalent microwave fields (2450 MHz frequency). Gas flow was maintained at 1 slm for each. Bed locations within each tube are denoted at the inlet and outlet, with span signified by an arrow along the wall. Note that each image was set on a common, discrete color scale for clarity. Original COMSOL images can be found in **Figure S4** (**Section S5**, ESI).

**Table 1** shows maximum, minimum, and average volume temperature in each modeled case, as well as associated absorbed power and heat loss. The absorbed power increased as the bed height increased for both 13 mm and 26 mm tube diameters. Radiative heat losses contributed significantly to the overall heat losses, which was around 50% – 60% for all bed height combinations at 13 mm tube diameter. Increasing tube diameter increased the heat losses significantly: over 90% of the heat was lost to radiation and convection in both 26 mm tubes, nearly 70% higher than their equal-height 13 mm counterparts. This finding also holds volumetrically: the 13-by-279.4 mm bed and 26-by-76.2 mm bed hold similar volumes (37.1 mL and 40.5 mL, respectively), while the latter's energy losses (91%) exceed the former's (55%) by 65.5%. In comparison with the 13 mm tubes, more of the heat losses experienced in the 26 mm tubes were radiative. Indeed, in the 13 mm diameter beds, the 76.2 mm and 279.4 mm tall beds see radiative-to-convective heat loss ratios of 2.58 and 1.97, respectively, while the corresponding-height beds in the 26 mm diameter tube experience ratios of 2.84 and 2.99, respectively. The ratio is 44.2% higher in the 26 mm

tube for the corresponding-volume cases (the 13-by-279.4 mm and 26-by-76.2 mm beds) and total radiative losses as a proportion of the total is 81.1% higher in the wider tube, indicating radiative heat loss is more dominant. While wider diameters alter field distribution and necessitate different power requirements, different absorbed power levels were not associated with higher proportions of radiation. The increase in radiation is, therefore, solely attributable to the temperature gradients that arise from the difference in geometry. This is contrary to expectation, as radiative heat loss is a surface phenomenon and the surface-area-to-volume ratio of the 26 mm tube (1.80 $cm^{-1}$) is significantly lower than the 13 mm tube (3.15 $cm^{-1}$) for corresponding-volume beds.[36] However, in accordance with the Stefan-Boltzmann law of radiation (**Section S8**, ESI),[37] there is a greater contribution from temperature gradients (within a thermal mass and between the mass and its surroundings) to radiative heat transfer than from surface area. 26 mm test cases have both wider temperature ranges and average temperatures, resulting in far greater heat losses.

**Table 1.** Maximum, minimum and average volume temperatures for varying catalyst bed height.

| Reactor Tube Diameter (mm) | Bed Height (mm) | Temperature Range (°C) | Average Temperature (°C) | Total Absorbed Power (W) | Radiative Heat Loss | | Convective Heat Loss | | Total Heat Loss | |
|---|---|---|---|---|---|---|---|---|---|---|
| | | | | | (W) | % of total | (W) | % of total | (W) | % of total |
| 13 | 19.0 | 251.2 - 310.5 | 289.3 | 23.0 | 9.9 | 43% | 4.1 | 18% | 14.0 | 61% |
| 13 | 38.1 | 202.3 - 296.3 | 255.4 | 32.0 | 11.8 | 37% | 4.8 | 15% | 16.6 | 52% |
| 13 | 76.2 | 175.1 - 280.5 | 239.4 | 43.8 | 17.0 | 39% | 6.6 | 15% | 23.6 | 54% |
| 13 | 279.4 | 53.9 - 184.9 | 136.9 | 53.0 | 19.5 | 37% | 9.9 | 19% | 29.4 | 55% |
| 26 | 76.2 | 19.5 - 314.3 | 296.6 | 70.0 | 46.9 | 67% | 16.5 | 24% | 63.4 | 91% |
| 26 | 279.4 | 27.2 - 311.6 | 218.7 | 156.5 | 109.3 | 70% | 36.6 | 23% | 145.9 | 93% |

Overall, the modeling work has shown that increasing thermal mass or altering reactor geometry can influence attenuation profiles in a manner that is beyond what is predictable from dielectric catalyst properties alone since (1) field intensity must be spread over more catalyst, (2) larger beds experience non-uniform attenuation with a concentration in the vertical center, and (3) taller beds see a longer flow path where more conductive and convective heat transfer can occur. This results in temperature gradients that can affect performance. Namely, taller catalyst beds experienced increasingly severe thermal gradients with nonuniform electric field profiles. Moreover, although the 26 mm diameter catalyst bed should be within ideal penetration depth limits, it sees an altered temperature profile that can result in significant heat losses. Therefore, while microwave heating has the potential to create uniform electric fields and resulting temperature gradients, there are significant geometric restrictions to which a microwave reactor must

adhere. These findings are in the absence of reaction conditions, where elements like heat generated from the exothermic $NH_3$ synthesis reaction add an additional layer of complication that can worsen these nonuniformities. Experimentation is essential as the most direct way to evaluate these elements and how they change with scale.

### 2.3 Experimental Reactor Development

We began experimental work using the computational findings as a guide. A 13 mm tube was used for experimentation, along with a 2450 MHz frequency microwave source, to minimize heat losses at this scale while also maximizing attenuation and radial uniformity. A stoichiometric (3:1) gas mixture of $H_2$:$N_2$ was used for the entirety of the experimental work. General scale-up trends were first evaluated by incrementing catalyst mass under reacting gas flow while maintaining a constant GHSV (**Figure 4**). This method of analysis is common practice when comparing reactor systems of different scales, primarily because it is simple, intuitive, and on some levels necessary for characterization or performance prediction.[38] However, since parameters such as mass transfer rate, reactor volume, kinetic activity, or flow dynamics do not scale proportionally with each other,[39] reactors at different scales can be in different reactive states and conditions even if the space velocity is the same. As a result, performance can vary and deviate from prediction. Caution should, therefore, be used when relying solely on space velocity (or other dimensionless or partially dimensionless parameters) during scale-up procedures. Indeed, as catalyst mass (and, by extension, bed volume) increased in **Figure 4** with a constant space velocity, linear gas velocity increased, too (shown in the top panel). As a result, $H_2$ conversion increased steadily with catalyst mass up until about 2% conversion with 10 g of catalyst; this fairly linear increase in conversion with catalyst mass at a constant GHSV is indicative of an externally transport limited system.[40] Above 10 g of catalyst, the conversion plateaued at 2% (representing a transition to a kinetically limited regime at the same GHSV), owing to an increase in linear flow velocity that is necessary to maintain space velocity with larger catalyst volumes (supported by **Figure S7**, ESI). However, since gas velocity increases, gas particles flow through the reactive bed fast enough to keep up with the rate of reaction, resulting in increased $NH_3$ production even with the same normalized flow rate. This difference in flow regimes at different scales, and the resulting impact on total production, is key to scale-up and reactor development.

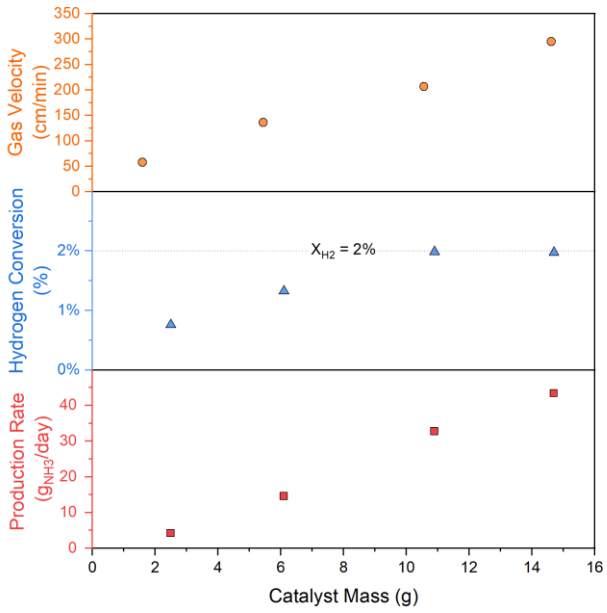


**Figure 4.** Performance of varying amounts of microwave-heated CsRu2-4%/$CeO_2$ (using a 2450 MHz frequency) at around 23 bar, 260°C, and subjected to a 3:1 $H_2$:$N_2$ flow at about 43,000 $hr^{-1}$. Gas velocity (cm/min, in the *top panel*), $H_2$ conversion (%, in the *center panel*), and total production rate ($g_{NH3}$/day, in the *bottom panel*) are reported with varying catalyst mass (g).

This was further evaluated through parametric optimization, where temperature and pressure were varied in 5 g and 10 g catalyst beds (5x and 10x increases from previous work, respectively[23]), with the goal of providing guiding trends for future scaling (**Figure 5**). The heights of the 5 g (red circles) and 10 g (blue diamonds) catalyst beds were about 19 mm and 38 mm, respectively. Additionally, equilibrium conversion of $H_2$ to $NH_3$ was calculated using Shacham and Brauner's methodology (black solid line).[22] **Figure 5a** shows the influence of operating pressure on catalyst bed activity, where the catalyst beds were heated with microwave heating at 260°C in a 13 mm diameter tube under reacting gas flow (GHSV of around 70,000 $hr^{-1}$ and 40,000 $hr^{-1}$ for the 5 g and 10 g beds, respectively). Different space velocities were used to ensure both beds were under a kinetically limited regime with the highest conversion at optimum activity (which is proportional to conversion for a given catalyst mass[41]) at STP conditions to allow accurate analysis, in accordance with the findings in **Figure 4** and **Figure S7** (ESI). Both beds experienced a monotonic increase in activity with pressure: microwave-induced $H_2$ conversion in the 5 g catalyst bed began around 0.03% at atmospheric pressure and gradually increased to about 0.51% at 22 bar, while the 10 g bed experienced an increase from 0.24% to 2.44%. This occurs because higher pressures increase equilibrium conversion by making $NH_3$ production more favorable (following Le Châtelier's Principle[9]), kinetically driving faster reactions, and lengthening residence times due to higher molecular gas densities,

enhancing conversion.[41] Increasing catalyst mass (here, from 5 g to 10 g) also leads to higher conversion by increasing the number of gas-catalyst interactions even when both beds are in a kinetically limited regime. Still, the calculated equilibrium is roughly one-to-two orders of magnitude larger than the corresponding microwave-induced conversion, indicating the potential for further improvement with scale. Nonetheless, microwave-induced conversion changes with pressure in a similar pattern to the equilibrium model, serving as evidence that the catalyst bed is reaching the potential dictated by its kinetic limit with no indication of any limitations at higher pressure.

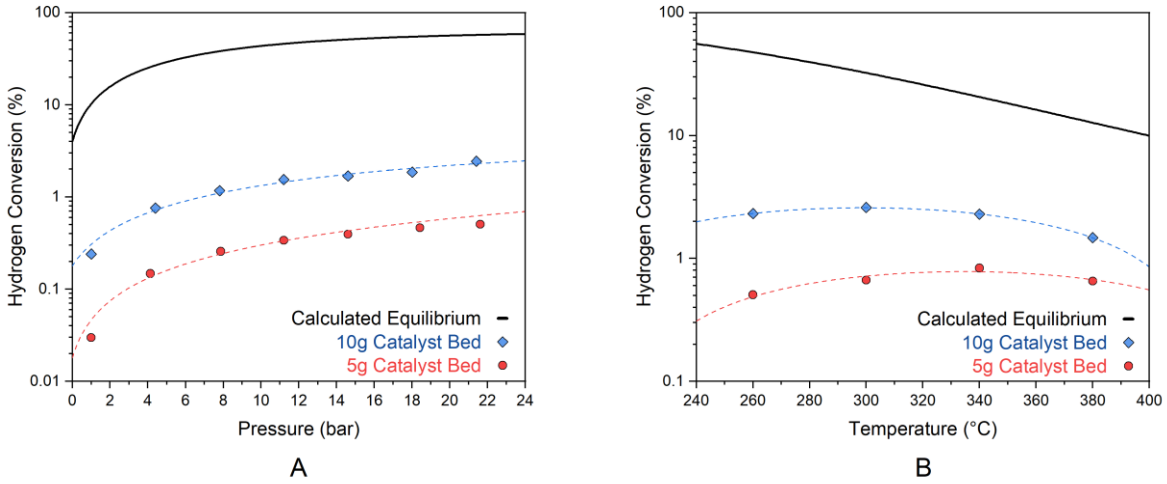


**Figure 5**. $H_2$ conversion (%), in log scale, for reacting gas (3:1 $H_2$:$N_2$ gas mix) flowing through CsRu2-4%/$CeO_2$ beds with loadings of 5.5 g (red circles, bed height: 19 mm, temperature: 260°C, GHSV: 70,000 $hr^{-1}$) and 10.1 g (blue diamonds, bed height: 38 mm, pressure: 22 bar, GHSV: 40,000 $hr^{-1}$), subjected to microwave heating (2450 MHz frequency) in a 13 mm quartz reaction tube. Different GHSVs ensured each bed was in a kinetically limited state with maximal activity at STP conditions. A reference black line is plotted for the modelled thermodynamic equilibrium conversion at each state. **(A)** Absolute pressure is varied while operating temperature is maintained at 260°C. **(B)** Operating temperature is varied while absolute pressure is maintained at 22 bar. Simple polynomial-fit curves (dashed lines) are displayed for each dataset for illustrative purposes.

Operating pressure only impacts activity by altering thermodynamic equilibrium. Conversely, operating temperature has an impact both on equilibrium and on activation energy, each of which have different impacts on catalytic activity. As such, operating temperature carries a more complex balance between kinetic performance and thermodynamic potential than operating pressure.[9] Calculated equilibrium $H_2$ conversion decreases steadily as temperature increases because it is only a model of thermodynamic equilibrium is not influenced by these kinetic principles (**Figure 5b**). In the 5 g bed at 22 bar, measured

conversion increases with temperature up to about 340°C, from 0.50% to 0.83%, and subsequently decreases to 0.65% as temperature further increases to 380°C. This is due to the kinetic requirements of the reaction, where lower temperatures are insufficient in providing activation energy for catalysis; once the requirement is sufficiently met (here, at 380°C), equilibrium becomes too limiting (seen in the decrease in the calculated value) and conversion begins to decrease. Importantly, the 10 g bed exhibits a similar behavior but shows a different optimal temperature: conversion increases from 2.32% to 2.60% at around 300°C (higher than the 5 g bed) and quickly decreases to about 1.47% at 380°C, decreasing at a faster rate to approach the conversion of the 5 g bed at that temperature. Since conversion is still significantly far from equilibrium (around 6% of the equilibrium value between 300°C and 380°C), a closer approach to equilibrium in the 10 g bed is not the likely cause of this early decrease in activity.[40] This drop in performance can be attributed to the variance of microwave field distribution and attenuation with bed height, modeled in **Figure 3**. Specifically, while the 19 mm tall reactor model (equivalent to the 5 g bed experimentally analyzed in **Figure 5**) showed relatively lower temperature deviation (temperature ranged from inlet to outlet was about 251.2°C to 310.5°C, a difference of 59.3°C, with a setpoint of 260°C at the center), deviation in the 38 mm case (equivalent to the 10 g bed) was more severe since the longer bed altered the attenuation profile and allowed more internal conductive heat exchange to occur. The temperature range increased to 94°C (202.2°C to 296.2°C) in the 10 g, 38 mm bed with the same gas flow rate (1 slm, equivalent to a GHSV of 12,000 $hr^{-1}$) and center temperature setpoint (260°C), a 58.5% increase. For this reason, the optimal temperature in the 10 g bed (300°C) is lower than the optimum in the 5 g bed (340°C), ensuring its wider temperature range optimally balances between the high and low temperature requirements of kinetics and thermodynamics, respectively (**Figure 5**). This signifies that a temperature gradient is already starting to impact reactor performance at this scale and must be addressed to advance further reactor development.

Nonetheless, this 10 g bed displayed promising performance upon further evaluation (**Figure 6**). Total $NH_3$ output and energy efficiency (**Section S2**, ESI) were analyzed as they are two essential performance statistics that dictate real-world viability. **Figure 6a** shows how total production rate and energy efficiency vary with GHSV at an operating pressure and temperature of 23 bar and 260°C, respectively. Production rate (red circles on the primary axis) increases rapidly and linearly with GHSV at lower flow rates (from $1*10^4$ to $4*10^4$ $hr^{-1}$), indicating the bed is externally transport limited. The slope begins to change around $4*10^4$ $hr^{-1}$, signifying the beginning of a transition to a kinetically limited regime at a production rate of around 53 $g_{NH3}$/day.[41] There is virtually no change in the production rate at flow rates higher than this (plateauing around 55 $g_{NH3}$/day), meaning that there is little to no benefit to increasing the GHSV past the initially kinetically limited point. This notion is furthered by the change in energy efficiency, which increases in the transport limited region in the same manner as production rate. However, energy

efficiency peaks (at around 45 $g_{NH3}$ produced per kWh of microwave energy) at the initially kinetically limited flow rate and quickly drops at higher flows as production remains constant while more microwave energy is required to counteract the cooling effects faster flowing reacting gas (first explored through modeling in **Figure S5** and confirmed experimentally in **Table S1**). The change in production rate and energy efficiency with temperature is shown in **Figure 6b** (operating pressure is 23 bar and GHSV is 40,000 $hr^{-1}$). Production rate increases to a peak (of about 42 $g_{NH3}$/day in the 280°C – 300°C temperature region) and decreases gradually at higher temperatures, in a way similar to **Figure 5b**. Energy efficiency also increases with temperatures to a peak of around 40 $g_{NH3}$/kWh at 280°C, but quickly decreases since there is no change in production while higher microwave power is required to maintain higher temperatures (**Figure S5** and **Table S1**). **Figure 6c** shows the influence of operating pressure, where production rate increases nearly monotonically with pressure. Since higher pressures require almost no additional microwave power (**Table S1**), energy efficiency increases in the same manner.

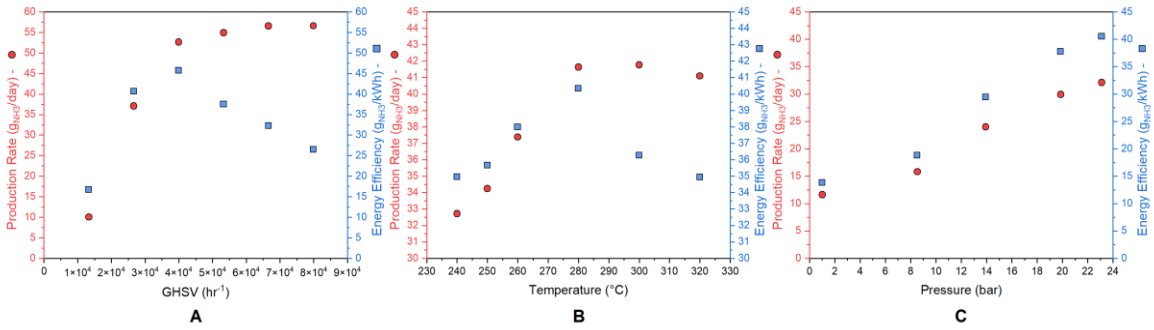


**Figure 6.** Influence of **(A)** GHSV ($hr^{-1}$), **(B)** Temperature (°C), and **(C)** Pressure (bar) on total production rate ($g_{NH3}$/day, red circles on primary axis) and energy efficiency ($g_{NH3}$/kWh, blue squares on secondary axis) of a 10 g bed of CsRu2-4%/$CeO_2$ (bed height: 38 mm) subjected to a continuous 3:1 $H_2$:$N_2$ reacting gas flow under microwave irradiation (2450 MHz frequency). Relevant conditions are: **(A)** pressure = 23 bar and temperature = 260°C, **(B)** pressure = 23 bar and GHSV = 40,000 $hr^{-1}$, and **(C)** temperature = 260°C and GHSV = 33,000 $hr^{-1}$.

The key achievements in this paper are the considerably high production rates that are matched by comparably high energy efficiencies. The highest $NH_3$ production rate observed in this paper is 56.6 $g_{NH3}$/day (at a GHSV, temperature, and pressure of 80,000 $hr^{-1}$, 260°C, and 23 bar, respectively) with a corresponding energy efficiency of 26.6 $g_{NH3}$/kWh. At a slightly lower gas flow rate, closer to the onset of kinetic limitation (at 40,000 $hr^{-1}$, 260°C, and 23 bar), the reactor operated with a production rate of 52.6 $g_{NH3}$/day and an energy efficiency of 45.7 $g_{NH3}$/kWh. Both of these production rates are the highest reported in literature for lab-scale alternative $NH_3$ synthesis processes (whether they use novel techniques and the

typical $H_2$:$N_2$ feedstock or unique synthesis routes altogether), to the best of our knowledge (**Figure 7**).[42-77] Moreover, this 52.6 $g_{NH3}$/day, 45.7 $g_{NH3}$/kWh datapoint operated with 3.19% $H_2$ conversion. While further scale-up is expected to increase this conversion, performance at this scale has already passed the 2% $H_2$ conversion threshold; below this figure, required energy input for $NH_3$ separations becomes significant.[13] Importantly, the use of microwave heating was essential in providing targeted heating with little wasted energy and more favorable operating conditions: the energy efficiency of 45.7 $g_{NH3}$/day is among the highest reported in literature. The only techniques reported to operate more efficiently are electrochemically driven reactors with production rates lower than 100 $\mu g_{NH3}$/day.[70, 76] While promising, these techniques are likely to suffer from the scaling limitations inherent to electrochemical $NH_3$ synthesis (due to limits in current density, reaction selectivity, and mass transport).[78] This represents a significant step forward in this field.

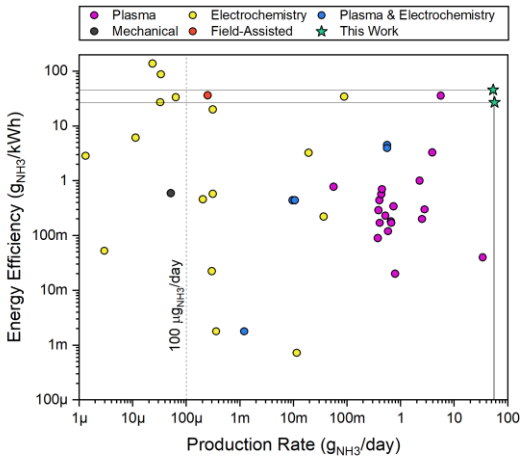


**Figure 7**. Performance from the scaled reactor in this work compared to recent literature on alternative $NH_3$ synthesis techniques.[42-77]

This energy efficiency is promising in comparison to Haber-Bosch's capabilities. Since the aim of this work is to enable small-scale, distributed $NH_3$ production, it is necessary to compare the present reactor to small-scale Haber-Bosch processes that are similar to this work's target in production capacity. Large-scale Haber-Bosch plants present an optimized case where large thermal masses and continuous production minimize energy losses; in this scenario, the heat generated by the reaction effectively catalyzes further reaction. This self-sustaining effect allows these reactors to overcome the theoretical maximum energy efficiency of 160 $g_{NH3}$/kWh and achieve efficiencies up to 781.3 $g_{NH3}$/kWh.[79] Conductive, convective, and radiative energy losses become more prevalent and problematic at smaller scales that are more appropriate for load-following with renewables: conventional small-scale Haber-Bosch synthesis loops (i.e., excluding

ancillary unit operations) operate at a total energy efficiency of about 75.8 $g_{NH3}$/kWh,[13] only about 65% higher than the benchmark achieved in this study. Importantly, these small-scale conventional synthesis loops still operate at production levels on the order of 10 $kg_{NH3}$/day compared to the present operation on the order of 10 $g_{NH3}$/day, roughly 3 orders of magnitude higher. Moreover, significant convective and radiative heat loss was found for this paper's reactor system, greater than 50% loss in all tested cases (**Table 1**). If just half of these heat losses can be eliminated at this scale, the energy efficiency of this reactor would grow from 48.7 to 65.6 $g_{NH3}$/kWh. This would only be about 15% lower than the 75.8 $g_{NH3}$/kWh efficiency achieved by small-scale Haber-Bosch synthesis unit operations without the additional conductive and convective insulation that comes with larger scales.

Microwave heating, therefore, provides a unique level of energy efficiency, along with highest-reported laboratory-scale production levels, that can be expected to improve with further reactor development and scale-up. It is, however, important to maintain performance through this effort, with chief focus placed on ensuring an optimal field attenuation profile and minimizing energy losses to enable efficient production. As reactor scales increase, penetration depth becomes more important than point-specific attenuation in ensuring a uniform field distribution. Therefore, a 915 MHz frequency may become more able to reduce gradients in temperature with less wasted energy. However, since microwave fields are hypothesized to have non-thermal (kinetic) contributions to a reaction, varying electromagnetic frequency may influence reaction kinetics. The incorporation of additional chemical components to the catalyst beds has also been found to tune penetration depth.[33] Moreover, heat loss can be minimized using established techniques, like equipment design or material choice and structuring.[80] For example, different reactor geometries can alter field profiles and influence uniformity and the flexibility of targeted microwave heating further expands possible design choices. These adjustments can halt development as much as they can provide avenues for improvement. As such, they must be a focus of further scale-up and development work, and can only be proven and optimized through a combination of numerical and experimental approaches.

## 3 Conclusion

Although this work has demonstrated a benchmark production rate with an energy efficiency unmatched by novel reactors of sufficient scale, it has already showcased the scientific and engineering challenges involved in scaling up microwave systems. While non-plasma microwave-heating offers several distinct benefits, including targeted heating, fast system response, and favorable operating conditions, scaling such systems comes with several unique challenges. Specifically, even with a kinetically optimized catalyst, dielectric catalyst properties govern interaction with microwave fields and dictate reactor geometry. This is compounded by the choice of microwave field properties, and the fact that the importance

of relevant variables (like field attenuation or penetration depth) change with scale. For example, a 2450 MHz was used this work for its superior attenuation, which limited the reactor to using narrow-diameter tubes. This has significant implications on microwave field distribution. Even at the mid-phase laboratory scale investigated in this paper, electric fields must spread more over the increased volume, reducing the specific field intensity at any point. Compounded by internal heat conduction throughout the length of the catalyst bed, severe temperature gradient formation can already impact performance. Variations of tube diameter and gas flow rate experience similar results, where wider diameters distribute equivalent electric fields over more space in the same manner as taller catalyst beds and higher gas flow rates increase convective heat loss regardless of field strength; both necessitate stronger electric fields. Variation of tube diameter can even impart heat losses that create a limitation more stringent than what was predicted from microwave penetration depth. Thus, further microwave field modeling in the presence of temperature-buildup abatement techniques is needed for further scale-up work.

Lastly, it is important to note that the conclusions drawn from this work are highly dependent on scale and reaction conditions. For instance, pressure drop was found to be negligible for the conditions in this study (**Section S13**, ESI), yet it can become more significant with higher gas flow rates or longer flow paths. Moreover, as observed experimentally and confirmed numerically, temperature gradients and microwave field distributions are highly dependent on reactor geometry. Different catalysts may also possess different dielectric properties, which may alter the applicability of these conclusions. While this work can guide scale-up activities, particularly in regards to microwave-driven processes, caution should be used to ensure these principles and conclusions remain applicable with every significant change in scale or operation.

## 4 Materials and Methods

### 4.1 Catalyst Preparation

Cerium (IV) oxide (99.95%, $CeO_2$, Sigma-Aldrich), Ruthenium (III) nitrosylnitrate (≥31.3% Ru, $Ru(NO)(NO_3)_3$, Alfa Aesar), Cesium nitrate (99.8%, $CsNO_3$, Alfa Aesar), were used to synthesize the catalysts. All chemicals used in this work were purchased from the commercial suppliers and used as received without any further purification. All catalysts were prepared by a wet-impregnation method, where the $CeO_2$ support was wet impregnated with a solution of $Ru(NO)(NO_3)_3$ and $CsNO_3$. After drying in air (80°C, 12 h), the sample was calcined at 550°C for 4 h. The catalyst thus obtained had a nominal 4 wt.% content of Ru and 2 wt.% Cs. More details on the synthesis method and the composition, including characterization, can be found in previous work from this group.[23] Catalyst particles were sized using a Fieldmaster Metal Sieve Set to particulate sizes no greater than 500 μm. This size was chosen based on best practices to avoid channeling or back-mixing.[38, 40]

### 4.2 Characterization

SEM imaging was performed on fresh catalyst using a Hitachi SU-1500 Scanning Electron Microscope, operating at 15 kV with a vacuum pressure of about $10^{-6}$ Torr. Powered sample was adhered to a standard Hitachi stage using PELCO® Colloidal Graphite in isopropanol base (20 wt.%, Ted Pella, Inc.), cured in atmosphere at ambient conditions.

Dielectric property measurements were carried out using a cavity perturbation technique in a $TM_{010}$ cavity system, developed and carried out by Microwave Properties North in Ontario, Canada. The system is described in great detail by Hutcheon, et al.[81] Samples are heated resistively to specified setpoint temperatures and rapidly moved into a microwave cavity, where they are perturbed by mild electromagnetic fields at varying frequencies to allow dielectric property measurements. About 0.5 g of catalyst was packed into an amorphous silica holder using a uniaxial press with a pressure of about 1,240 bar. Measurements were carried out in a reducing atmosphere (4% $H_2$ in Ar), flowing at 10 sccm. Temperature stepped up from room temperature to 260°C and dwelled for 1 hr to promote reduction. Temperature then returned to room temperature, stepped up to 600°C (the linear sweep reported in this study), and finally returned to room temperature again. Following measurement, the empty sample holder was run to measure background. No contamination was found during this step.

### 4.3 Numerical Modeling

A Multiphysics numerical model was developed using COMSOL Multiphysics software to predict the heating profile and temperature range inside the catalyst bed with change in catalyst bed height and reactor tube diameter. The model was experimentally validated. Further details of the model's governing equations[34] and boundary conditions, including the use of the Nyquist Critereon,[34] can be found in **Section S12** (ESI).

A 3-D geometry of the microwave cavity used in this paper (the H-Field cavity) was created in COMSOL 5.6 (**Figure S1**). The geometry consisted of a coaxial input port, an aluminum WR340 standard waveguide (0.086 m height, 0.043 m wide) shorted at the far end and fitted with an aluminum sliding short as shown in **Figure S1**. The H-Field circular cavity was made of aluminum and 104 mm in diameter. The quartz reactor tubes of varying diameters could fit through the cavity vertically. The powdered catalyst bed was modeled as a porous material inside the reactor tube. The waveguide and sliding short material were assumed to be bulk aluminum while the reactor tube was defined as a quartz glass material. Waveguide void was assumed to be filled with air at standard temperature and pressure. Default COMSOL values for air, aluminum and quartz glass were used for the model. The dielectric properties of catalyst material were measured as a function of temperature at 2450 MHz frequency. Since the dielectric constant did not change

significantly from room temperature, constant values were used (**Figure 1b**). The thermal properties of the catalyst were obtained from literature. The CsRu2-4%/$CeO_2$ catalyst material has an electrical conductivity of 0.32 S/m, an average relative permittivity of 11.57, a thermal conductivity of 6 W/mK, a density of 7,000 kg/$m^3$, and a constant pressure heat capacity of 710 J/kgK. Correspondingly, the quartz glass that houses the catalyst has an electrical conductivity of $1 * 10^{-14}$ S/m, an average relative permittivity of 4.2, a thermal conductivity of 1.4 W/mK, a density of 2,210 kg/$m^3$, and a constant pressure heat capacity of 730 J/kgK.[82]

### 4.4 Reactor Design & Operation

Microwave experiments were performed using a 2.45 GHz (200 W) solid-state mono-mode 2450 MHz microwave generator from Sairem (model GMS200). A reactor (the H-Field cavity) was designed and provided by Malachite Technologies, Inc. (**Figure S1**). The reactor was pressurized using a downstream back pressure regulator (not pictured), and ProSense DPG1-600 pressure gauges were placed at the inlet and outlet of the chamber to determine relevant pressure values. Pressure drop was found to be minimal (**Section S12**, ESI) for gas flow through the reactor's catalyst bed for the operating scope of this study, thereby ensuring a consistently accurate determination of pressure.

The reactions were carried out using a temperature-control loop with maximum power set at 200 W. Stub tuners, a sliding short circuit, and variable frequency (between 2.4 GHz and 2.5 GHz) were used to minimize reflected power. The forward and reflective powers during the reaction was recorded continuously. All reported data in this paper occurred with 0 W reflected power. A quartz tube with a 13 mm internal diameter was placed inside the microwave cavity to house the catalyst. The temperature was primarily measured using an IR pyrometer from Micro-Epsilon (model CTLM3), with a temperature range from 100°C to 625°C. This pyrometer setup allowed for the temperature reading from the side of the sample surface. A Teledyne FLIR Systems IR Camera (Model SC 6000, Type 640x512-pixel InSb mid-wave IR) was used for thermal imaging (in **Section S2**, ESI), and corresponding analysis was conducted using the associated FLIR ResearchIR 4 software. Both the pyrometer and FLIR camera were calibrated against an external reference to ensure accurate temperature reading. A sapphire window was fitted to the top of the reactor (at point "F" on **Figure S1**) so that the FLIR camera could observe the catalyst during operation.

The standard CsRu2-4%/$CeO_2$ catalyst was used for each reaction while flowing a 3:1 stoichiometric mixture of $H_2$ and $N_2$ with a fixed flow rate through the quartz tube. Reduction of catalyst samples was carried out in the microwave reactor at 260°C for 1 hr using the necessary microwave power for the Ru based catalyst with the synthesis gas flowing at 1 slm. All reported reaction data in this paper is post-reduction. The exit gas stream ($H_2$, $N_2$, $H_2O$, and $NH_3$) was analyzed using a Honeywell Manning AirScan IR-F9-0/2%-N1 NH3 Sensor, which can measure $NH_3$ composition in a gas stream using an IR

sensor at a parts per million (ppm) level. The $NH_3$ production was represented as grams of $NH_3$ produced per gram of catalyst per hour and was calculated using the average ppm recorded by the IR sensor.

## Author contributions

SGM and CW were responsible for the paper's theme and conceptualization. SGM carried out experimental work and PM carried out computational work; together, SGM and PM formed the methodology. CW, RW, and JH provided supervision. SGM and PM prepared the original manuscript, while SGM, PM, BD, and CW conducted document review and editing steps.

## Competing interests

All authors declare no competing interests.

## Acknowledgments

The authors would like to thank Microwave Properties North for conducting dielectric properties measurements of our catalyst. This research was supported by DOE ARPA-E under Award No.: DE-AR0000807.

## 5 References

1. NREL, Best Research Cell Efficiencies, https://www.nrel.gov/pv/cell-efficiency.html).
2. S. L. Moffitt, L. T. Schelhas, S. Melkote and M. F. Toney, in *Advanced Micro- and Nanomaterials for Photovoltaics*, eds. D. Ginley and T. Fix, Elsevier, 2019, DOI: 10.1016/b978-0-12-814501-2.00007-4, pp. 153-173.
3. X. Wu, Y. Hu, Y. Li, J. Yang, L. Duan, T. Wang, T. Adcock, Z. Jiang, Z. Gao, Z. Lin, A. Borthwick and S. Liao, *Renewable and Sustainable Energy Reviews*, 2019, **104**, 379-393.
4. McKinsey & Company and LDES Council, *Net-zero power: Long-duration energy storage for a renewable grid*, 2021.
5. A. Valera-Medina, H. Xiao, M. Owen-Jones, W. I. F. David and P. J. Bowen, *Prog. Eng. Comb. Sci.*, 2018, **69**, 63-102.
6. D. R. MacFarlane, P. V. Cherepanov, J. Choi, B. H. R. Suryanto, R. Y. Hodgetts, J. M. Bakker, F. M. Ferrero Vallana and A. N. Simonov, *Joule*, 2020, **4**, 1186-1205.
7. D. DeSantis, B. D. James, C. Houchins, G. Saur and M. Lyubovsky, *iScience*, 2021, **24**, 103495.
8. C. Smith, A. K. Hill and L. Torrente-Murciano, *Energy & Environmental Science*, 2020, **13**, 331-344.
9. M. Appl, in *Ammonia: Principles and Industrial Practice*, Weinheim: Wiley-VCH, 1999, DOI: 10.1002/9783527613885, ch. 3.
10. K. Verleysen, A. Parente and F. Contino, *Energy*, 2021, **232**, 121016-121016.
11. V. Kyriakou, I. Garagounis, A. Vourros, E. Vasileiou and M. Stoukides, *Joule*, 2020, **4**, 142-158.
12. International Energy Agency, *Ammonia Technology Roadmap*, 2021.
13. K. H. R. Rouwenhorst and L. Lefferts, *Catalysts*, 2020, **10**, 1-19.
14. M. H. Vu, M. Sakar, S. A. Hassanzadeh-Tabrizi and T. O. Do, *Advanced Materials Interfaces*, 2019, **6**, 1900091-1900091.

15. A. Ramirez, J. L. Hueso, M. Abian, M. U. Alzueta, R. Mallada and J. Santamaria, *Sci Adv*, 2019, **5**, eaau9000.
16. T. Ano, S. Tsubaki, A. Liu, M. Matsuhisa, S. Fujii, K. Motokura, W.-J. Chun and Y. Wada, *Communications Chemistry*, 2020, **3**, 2-12.
17. A. H. White and W. Melville, *Journal of the American Chemical Society*, 2002, **27**, 373-386.
18. V. Palma, D. Barba, M. Cortese, M. Martino, S. Renda and E. Meloni, *Catalysts*, 2020, **10**, 246-246.
19. J. Hu, C. Wildfire, A. E. Stiegman, R. A. Dagle, D. Shekhawat, V. Abdelsayed, X. Bai, H. Tian, M. B. Bogle, C. Hsu, Y. Luo, S. D. Davidson and Y. Wang, *Chem. Eng. Journal*, 2020, **397**, 125388.
20. A. Nielsen, *Ammonia*, Springer Berlin, Heidelberg, 1995.
21. Y. Wang, T. S. Khan, C. Wildfire, D. Shekhawat and J. Hu, *Cat.Comm.*, 2021, **159**, 106344-106344.
22. M. Shacham and N. Brauner, *Edu. Chem. Eng.*, 2015, **13**, 17-23.
23. Y. Wang, C. Wildfire, T. S. Khan, D. Shekhawat, J. Hu, P. Tavadze, R. Quiñones-Fernández and S. Moreno, *Chem. Eng. Journal*, 2021, **425**, 130546-130546.
24. C. Wildfire, V. Abdelsayed, D. Shekhawat and M. J. Spencer, *Cat.Comm.*, 2018, **115**, 64-67.
25. T. Van Gerven and A. Stankiewicz, *Industrial & Engineering Chemistry Research*, 2009, **48**, 2465-2474.
26. P. Yan, A. I. Stankiewicz, F. Eghbal Sarabi and H. Nigar, *Chemical Engineering Science*, 2021, **232**, 116383-116383.
27. H. Goyal, A. Mehdad, R. F. Lobo, G. D. Stefanidis and D. G. Vlachos, *Industrial & Engineering Chemistry Research*, 2019, **59**, 2516-2523.
28. E. Pert, Y. Carmel, A. Birnboim, T. Olorunyolemi, D. Gershon, J. Calame, I. K. Lloyd and O. C. Wilson, *Journal of the American Ceramic Society*, 2004, **84**, 1981-1986.
29. Teledyne FLIR, *Journal*, 2021.
30. S. P. Borodai and T. A. Betina, *Journal of Applied Spectroscopy*, 1988, **48**, 92-97.
31. A. Ken-ichi, K. Toshikazu, M. Shuzo and O. Takaharu, *Bulletin of the Chemical Society of Japan*, 1990, **63**, 1221-1225.
32. J. Lin, L. Zhang, Z. Wang, J. Ni, R. Wang and K. Wei, *Journal of Molecular Catalysis A: Chemical*, 2013, **366**, 375-379.
33. M. Morte, J. Dean, H. Kitajima and B. Hascakir, *Energy & Fuels*, 2019, **33**, 6327-6334.
34. P. D. Muley and D. Boldor, *J Microw Power Electromagn Energy*, 2012, **46**, 139-162.
35. Federal Communications Commission, 47 C.F.R. § 2.106, https://transition.fcc.gov/oet/spectrum/table/fcctable.pdf).
36. F. Di Natale, R. Nigro and F. Scala, in *Fluidized Bed Technologies for Near-Zero Emission Combustion and Gasification*, ed. F. Scala, Woodhead Publishing, 2013, DOI: https://doi.org/10.1533/9780857098801.1.177, pp. 177-253.
37. D. D. Ganji, Y. Sabzehmeidani and A. Sedighiamiri, in *Nonlinear Systems in Heat Transfer*, eds. D. D. Ganji, Y. Sabzehmeidani and A. Sedighiamiri, Elsevier, 2018, DOI: https://doi.org/10.1016/B978-0-12-812024-8.00003-5, pp. 105-151.
38. J. Worstell, *Adiabatic Fixed-Bed Reactors: Practical Guides in Chemical Engineering*, 2014.
39. N. Cherkasov, P. Denissenko, S. Deshmukh and E. V. Rebrov, *Chem. Eng. Journal*, 2020, **379**, 122292-122292.
40. C. Perego, *Catalysis Today*, 1999, **52**, 133-145.
41. H. S. Fogler, *Elements of Chemical Reaction Engineering*, Prentice Hall, Philadelphia, PA, 2016.
42. Y. Wang, M. Craven, X. Yu, J. Ding, P. Bryant, J. Huang and X. Tu, *ACS Catal*, 2019, **9**, 10780-10793.
43. B. H. R. Suryanto, D. Wang, L. M. Azofra, M. Harb, L. Cavallo, R. Jalili, D. R. G. Mitchell, M. Chatti and D. R. MacFarlane, *ACS Energy Letters*, 2018, **4**, 430-435.

44. J. Sun, D. Alam, R. Daiyan, H. Masood, T. Zhang, R. Zhou, P. J. Cullen, E. C. Lovell, A. Jalili and R. Amal, *Energy & Environmental Science*, 2021, **14**, 865-872.
45. Y. Gorbanev, E. Vervloessem, A. Nikiforov and A. Bogaerts, *ACS SC&E*, 2020, **8**, 2996-3004.
46. P. Lamichhane, B. C. Adhikari, L. N. Nguyen, R. Paneru, B. Ghimire, S. Mumtaz, J. S. Lim, Y. J. Hong and E. H. Choi, *Plasma Sources Science and Technology*, 2020, **29**, 045026-045026.
47. S. Kumari, S. Pishgar, M. E. Schwarting, W. F. Paxton and J. M. Spurgeon, *Chem Commun (Camb)*, 2018, **54**, 13347-13350.
48. H.-H. Kim, Y. Teramoto, A. Ogata, H. Takagi and T. Nanba, *Plasma Processes and Polymers*, 2017, **14**, 1-9.
49. R. Hawtof, S. Ghosh, E. Guarr, C. Xu, R. Mohan Sankaran and J. N. Renner, *Sci Adv*, 2019, **5**, eaat5778.
50. J. Wang, L. Yu, L. Hu, G. Chen, H. Xin and X. Feng, *Nat Commun*, 2018, **9**, 1795.
51. T. Mizushima, K. Matsumoto, H. Ohkita and N. Kakuta, *Plasma Chemistry and Plasma Processing*, 2006, **27**, 1-11.
52. G. Akay and K. Zhang, *Industrial & Engineering Chemistry Research*, 2017, **56**, 457-468.
53. J. Shah, T. Wu, J. Lucero, M. A. Carreon and M. L. Carreon, *ACS SC&E*, 2018, **7**, 377-383.
54. M. Iwamoto, M. Akiyama, K. Aihara and T. Deguchi, *ACS Catalysis*, 2017, **7**, 6924-6929.
55. J. Hong, M. Aramesh, O. Shimoni, D. H. Seo, S. Yick, A. Greig, C. Charles, S. Prawer and A. B. Murphy, *Plasma Chemistry and Plasma Processing*, 2016, **36**, 917-940.
56. M. L. Carreon, *Journal of Physics D: Applied Physics*, 2019, **52**, 483001-483001.
57. J. Shah, W. Wang, A. Bogaerts and M. L. Carreon, *ACS Applied Energy Materials*, 2018, **1**, 4824-4839.
58. J. Shah, J. Harrison and M. Carreon, *Catalysts*, 2018, **8**.
59. J. Nakajima and H. Sekiguchi, *Thin Solid Films*, 2008, **516**, 4446-4451.
60. K. Han, J. Luo, J. Chen, B. Chen, L. Xu, Y. Feng, W. Tang and Z. L. Wang, *Microsyst Nanoeng*, 2021, **7**, 7.
61. R. Manabe, H. Nakatsubo, A. Gondo, K. Murakami, S. Ogo, H. Tsuneki, M. Ikeda, A. Ishikawa, H. Nakai and Y. Sekine, *Chem Sci*, 2017, **8**, 5434-5439.
62. T. Mizushima, K. Matsumoto, J.-i. Sugoh, H. Ohkita and N. Kakuta, *Applied Catalysis A: General*, 2004, **265**, 53-59.
63. A. Gómez-Ramírez, A. M. Montoro-Damas, J. Cotrino, R. M. Lambert and A. R. González-Elipe, *Plasma Processes and Polymers*, 2017, **14**, 1600081-1600081.
64. P. Peng, Y. Li, Y. Cheng, S. Deng, P. Chen and R. Ruan, *Plasma Chemistry and Plasma Processing*, 2016, **36**, 1201-1210.
65. K. Aihara, M. Akiyama, T. Deguchi, M. Tanaka, R. Hagiwara and M. Iwamoto, *Chem Commun (Camb)*, 2016, **52**, 13560-13563.
66. A. Gómez-Ramírez, J. Cotrino, R. M. Lambert and A. R. González-Elipe, *Plasma Sources Science and Technology*, 2015, **24**.
67. B. L. Sheets and G. G. Botte, *Chem Commun (Camb)*, 2018, **54**, 4250-4253.
68. J. Nash, X. Yang, J. Anibal, J. Wang, Y. Yan and B. Xu, *Journal of The Electrochemical Society*, 2017, **164**, F1712-F1716.
69. B. H. R. Suryanto, K. Matuszek, J. Choi, R. Y. Hodgetts, H. L. Du, J. M. Bakker, C. S. M. Kang, P. V. Cherepanov, A. N. Simonov and D. R. MacFarlane, *Science*, 2021, **372**, 1187-1191.
70. J. Kong, A. Lim, C. Yoon, J. H. Jang, H. C. Ham, J. Han, S. Nam, D. Kim, Y.-E. Sung, J. Choi and H. S. Park, *ACS SC&E*, 2017, **5**, 10986-10995.
71. N. Lazouski, M. Chung, K. Williams, M. L. Gala and K. Manthiram, *Nature Catalysis*, 2020, **3**, 463-469.
72. N. Lazouski, Z. J. Schiffer, K. Williams and K. Manthiram, *Joule*, 2019, **3**, 1127-1139.
73. H. K. Lee, C. S. L. Koh, Y. H. Lee, C. Liu, I. Y. Phang, X. Han, C. K. Tsung and X. Y. Ling, *Sci Adv*, 2018, **4**, eaar3208.

74. K. Kim, C.-Y. Yoo, J.-N. Kim, H. C. Yoon and J.-I. Han, *Journal of The Electrochemical Society*, 2016, **163**, F1523-F1526.
75. S. Z. Andersen, V. Colic, S. Yang, J. A. Schwalbe, A. C. Nielander, J. M. McEnaney, K. Enemark-Rasmussen, J. G. Baker, A. R. Singh, B. A. Rohr, M. J. Statt, S. J. Blair, S. Mezzavilla, J. Kibsgaard, P. C. K. Vesborg, M. Cargnello, S. F. Bent, T. F. Jaramillo, I. E. L. Stephens, J. K. Norskov and I. Chorkendorff, *Nature*, 2019, **570**, 504-508.
76. F. Zhou, L. M. Azofra, M. Ali, M. Kar, A. N. Simonov, C. McDonnell-Worth, C. Sun, X. Zhang and D. R. MacFarlane, *Energy & Environmental Science*, 2017, **10**, 2516-2520.
77. G. F. Chen, X. Cao, S. Wu, X. Zeng, L. X. Ding, M. Zhu and H. Wang, *J Am Chem Soc*, 2017, **139**, 9771-9774.
78. J. H. Montoya, C. Tsai, A. Vojvodic and J. K. Norskov, *ChemSusChem*, 2015, **8**, 2180-2186.
79. B. Lin, T. Wiesner and M. Malmali, *ACS SC&E*, 2020, **8**, 15517-15531.
80. C. K. Ho, J. M. Christian, J. D. Ortega, J. Yellowhair, M. J. Mosquera and C. E. Andraka, presented in part at the SPIE High and Low Concentrator Systems for Solar Energy Applications IX, United States, 2014.
81. R. Hutcheon, M. d. Jong and F. Adams, *Journal of Microwave Power and Electromagnetic Energy*, 1992, **27**, 87-92.
82. K. Suzuki, M. Kato, T. Sunaoshi, H. Uno, U. Carvajal-Nunez, A. T. Nelson and K. J. McClellan, *Journal of the American Ceramic Society*, 2018, **102**, 1994-2008.